

Experimental investigation of a HOPG crystal fan for x-ray fluorescence molecular imaging

Tanja Rosentreter¹, Bernhard Müller², Helmut Schlattl¹, Christoph Hoeschen^{1,2}

¹Helmholtz Zentrum München, Research Unit Medical Radiation Physics and Diagnostics,
Ingolstädter Landstraße 1, 85764 Neuherberg, Germany

²Otto-von-Guericke-Universität Magdeburg, Department of Electrical Engineering and Information
Technology,
Universitätsplatz 2, 39106 Magdeburg, Germany

ABSTRACT

Imaging x-ray fluorescence generally generates a conflict between the best image quality or highest sensitivity and lowest possible radiation dose. Consequently many experimental studies investigating the feasibility of this molecular imaging method, deal with either monochromatic x-ray sources that are not practical in clinical environment or accept high x-ray doses in order to maintain the advantage of high sensitivity and producing high quality images.

In this work we present a x-ray fluorescence imaging setup using a HOPG crystal fan construction consisting of a Bragg reflecting analyzer array together with a scatter reducing radial collimator. This method allows for the use of polychromatic x-ray tubes that are in general easily accessible in contrast to monochromatic x-ray sources such as synchrotron facilities. Moreover this energy-selecting device minimizes the amount of Compton scattered photons while simultaneously increasing the fluorescence signal yield, thus significantly reducing the signal to noise ratio.

The aim is to show the feasibility of this approach by measuring the Bragg reflected K_{α} fluorescence signal of an object containing an iodine solution using a large area detector with moderate energy resolution. Contemplating the anisotropic energy distribution of background scattered x-rays we compare the detection sensitivity, applying two different detector angular configurations. Our results show that even for large area detectors with limited energy resolution, iodine concentrations of 0.12 % can be detected. However, the potentially large scan times and therefore high radiation dose need to be decreased in further investigations.

Keywords: x-ray fluorescence, molecular imaging, high-Z tracers, HOPG, diffraction on crystals

1 INTRODUCTION

X-ray computed tomography (CT) is one of the most important absorption-based imaging modalities in clinical practice today, when it comes to diagnostics, assessment of diseases, or treatment planning. Supplementary advances in image quality and contrast is generated via the application of contrast agents consisting of high Z-elements such as iodine, gold, or gadolinium. Generally the penetration depth of radiation in material correlates with the photon energy, resulting in a continuous decrease of x-ray absorption. One exception is the K-edge, characterized by a sudden discrete and discontinuous increase in x-ray attenuation. Taking advantage of this phenomenon can significantly raise the x-ray absorption efficiency when the x-ray source is adjusted to the K-edge. For high-Z elements the energy of this absorption edge in the diagnostic x-ray energy range of a few 10 keV, which makes it exploitable for imaging biological probes¹. Aiming to supply x-ray CT with functional and molecular imaging capability, goldnanoparticles (AuNPs) have been of particular focus in recent research due to their biocompatibility²⁻⁴. At the expense of high tracer concentrations and x-ray doses, AuNPs have nevertheless been successfully conjugated to certain bio-molecules, consequently delivering

reconstruction images of specific tumors⁵⁻⁷. However, for dose efficient imaging of very low contrast agent concentrations, absorption-based methods are limited in their detection sensitivity.

To resolve this deficiency x-ray fluorescence computed tomography (XFCT) has been introduced e.g. for iodine⁸⁻¹⁰ and gold¹¹⁻¹⁶, as an imaging technique which combines CT imaging with x-ray fluorescence (XRF), a method used for material analysis. Simulation studies comparing K-edge absorption CT with XFCT suggest that for imaging of very low tracer concentrations the latter provides a significantly higher sensitivity^{11,16}. In XRF an object containing a high-Z tracer distribution is irradiated by a x-ray source, inducing an excitation of the tracer's atoms followed by an emission of secondary x-rays (x-ray fluorescence), which are then detected by energy-resolving detectors, traditionally placed in a 90° angle to the x-ray source. Measuring in the beamline would not only lead to an increased detection of background scatter, but also create count-rate problems, since contributions of the primary beam would obscure the fluorescent signal. In the recorded spectrum, the energies of XRF photons and those of background scatter can be spectrally discriminated, so that quantitative information about the elemental composition of the sample can be derived. First studies of XRF in medical environment were carried out in synchrotron facilities in order to determine the quantity of different tracer agents in breast tissue¹⁷⁻¹⁹. A more recent study using a standard CT source, which in terms of availability and cost is to be preferred over synchrotron radiation sources, showed that, AuNP concentrations of down to 0.1 % could be detected²⁰.

In XFCT multiple XRF spectra from different angular projections are acquired and used to reconstruct 3D images of the contrast agent within a sample. Initially XFCT was performed with synchrotron sources²¹ because of their ability to provide monoenergetic x-ray radiation. Using monochromatic radiation reduces the detection of single- and multiple scattered Compton photons, which are significantly responsible for obscuring the XRF signal. Current research, however, is generally limited to conventional CT resources with regard to its applicability in routine biomedical imaging. Recent experiments have shown promising advances in sensitivity^{12,22} where concentrations of AuNPs of down to 0.25 % could be detected. Another study delivered quantitative estimates as well as 3D images of AuNP concentrations within the kidney and tumor of a mouse, albeit lengthy scan times and radiation doses far too high for clinical imaging²³. A fundamental challenge in XFCT imaging is the suppression of Compton scattering which may lead to count rate problems of the detector and is responsible for obscuring the XRF signal that consequently leads to an insufficient signal-to-noise ratio (SNR) and hence a decrease in sensitivity. The strength of the fluorescence signal can however be influenced by the angular position of the detector, due to the anisotropic angular-energy distribution of Compton scattering. Installing the detector in the backscatter region within the experimental setup results in an increase of XRF detection of up to 10 times, compared to the classical 90° detector position^{22,24,25}.

The choice of the detector itself plays a pivotal role for x-ray fluorescence imaging. It is advantageous to integrate detectors with a high energy resolution, since the ability of being able to separate the fluorescence signal from the Compton background is crucial for XRF imaging. The major drawback is that detectors with this property, such as HPGe and CdTe detectors, are generally limited in terms of maximum count rate and their sensitive area. With x-ray fluorescence being emitted isotropically this is problematic considering the immense loss of fluorescence information followed by an increased demand for radiation dose when solely covering a minimal fraction of the solid angle²⁶. In accordance with simulation studies, one approach to expand the angular coverage for dose efficient signal detection is to apply an array of multiple detectors with adequate detector resolution^{11,27}. Nevertheless, as stated above, the experimental implementation remains challenging as a result of the deficiency in energy resolution of currently available detectors with expanded sensitive area.

In order to address this problem we propose an imaging setup for XFCT together with an energy-selective analyzer crystal fan, which aims to compensate for the moderate energy resolution of large area detectors. This fan construction consists of radially arranged collimator leaves, filtering out non-radially directed multiple scattered x-rays, and an array of Bragg reflecting crystals functioning as additional energy filter. The energy selection of the x-rays prior to hitting the sensitive area of the detector minimizes the importance of the detector's energy resolution, which is why implementing the fan enables the application of large area detectors for increased solid angle coverage.

One of the first studies dealing with the combination of energy-selective crystals and the detection of x-ray fluorescence was proposed for synchrotron x-ray sources and performed with a single bent Laue crystal²⁸. The disadvantage besides the operation of an expensive synchrotron facility however, is the utilization of a single crystal, which due to its narrow reflectivity curve does not leave enough tolerance for angular deviations of incoming XRF photons. A more recent investigation conducted a proof-of-principle experiment implementing a HOPG (highly oriented pyrolytic graphite) crystal with mosaic structure²⁹, for the detection of K_α fluorescence photons of iodine¹⁰. At the expense of long acquisition times and high radiation doses, it was possible to detect an iodine concentration of down to 0.005 %, albeit with a CdTe detector with a superior energy resolution and small sensitive area. Additional analyses of the setup

including multiple radially directed energy-selective analyzer HOPG crystal leaves were simulated with the Monte Carlo Code Geant4³⁰, in order to estimate the minimal detectable iodine and AuNP concentration in small animals and humans respectively. The investigation was conducted for clinically applicable radiation doses, yet under the approximation of an idealized detector response and energy resolution^{10,31}.

In this work we resume the imaging scheme of the proof-of-principle experiment¹⁰ by investigating the practicality of the above stated array of five radially collimating and energy-selecting HOPG crystals together with a large area NaI detector with limited energy resolution. We proof the feasibility of this setup together with conventional polychromatic x-ray sources for the acquisition of iodine K_{α} XRF photons. We further compare reconstructed XFCT images of a phantom containing iodine as tracer agent that were recorded under two different detector positions and show that the backscatter configuration is advantageous for optimizing the detection sensitivity. Additionally expanding the detection area further improves the XRF signal yield and hence the SNR and potentially allows for further radiation dose reductions.

2 MATERIALS AND METHODS

The idea of the proposed imaging setup with analyzer crystal fan has evolved from a feasibility study with a single HOPG crystal¹⁰. As shown on the left side of figure 1, a pencil beam is generated by a filtered and collimated polychromatic x-ray source with a mean energy above the K-edge of iodine. This pencil beam is used to scan an object containing an iodine solution representing the molecular tracer. The pencil beam interacts with the iodine atoms via Photoelectric and Compton effect. In order to cover a large solid angle while measuring the fluorescence signal, it is advantageous to use a large area detector that would yet be very expensive when providing a high energy resolution. To still allow the discrimination of fluorescence photons the following setup is chosen where we implemented an analyzer crystal fan composed of five radially oriented blades, which consist of Aluminum and HOPG material (cp. r.h.s. of figure 1). The collimator reduces the amount of multiple scattered Compton photons, since these are dominantly directed non-radially, whereas fluorescence photons are not affected and proceed to the HOPG. The angle between the collimating part and the crystal part of the blade is set such that all radially directed x-rays that surmount the collimator enter and are reflected by the HOPG in the Bragg angle of the energy of the K_{α} fluorescence of iodine. Thus only x-rays near that energy are being Bragg reflected and directed towards the detector, and hence most single scattered photons are discarded. This energy-selective detection of iodine x-ray fluorescence eliminates the problems with count-rate limitations of the detector, even for larger objects and high x-ray fluxes.

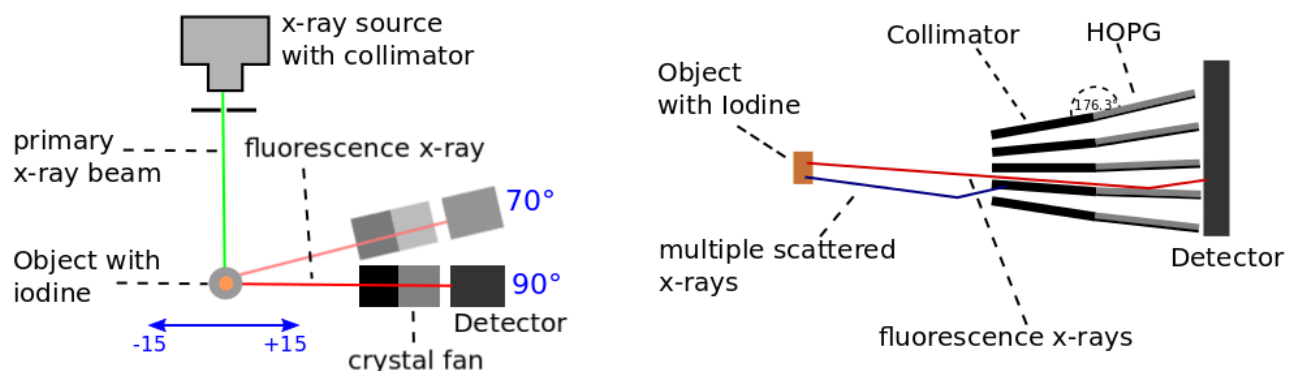


Figure 1: Left: Top view schematic of the x-ray fluorescence setup with analyzer crystal fan with 90° and 70° detector configuration; Right: Side view schematics of the HOPG crystal fan construction.

2.1 HOPG analyzer crystal

HOPG is an artificially produced mosaic crystal composed of layers of highly oriented pyrolytic graphite²⁹ (Optigraph, Berlin). The individual graphite crystallites are aligned to each other, such that the width of their angular distribution, or mosaic spread, is roughly 0.4° , giving the HOPG crystal an integrated reflectivity of up to 50% in the energy range between 20 and 30 keV. Mosaicity facilitates each photon of the incident energetic photon distribution to find a crystallite plane at the right Bragg angle, even if the angle of incidence to the crystal surface is fixed. The mosaic spread is also responsible for the width of the reflected energetic distribution, i.e. the energy resolution, which is notably reduced compared to monocrystals. This circumstance nonetheless allows for increased tolerance for otherwise narrow source size constraints. An advantage of HOPG material is that it can easily be bent to any shape since its crystallite structure releases stress on the material, as opposed to ideal crystals. Moreover, being increasingly used for monochromatization purposes³², it is known to additionally augment the intensity in the image plane due to the parafocusing effect³³.

The basis for studying the diffraction on crystal lattices, is the Bragg condition

$$2d \sin(\theta) = n \lambda, \quad (1)$$

where θ specifies the angle of incidence to the crystal surface (Bragg angle), d the spacing between lattice planes, λ the wavelength, and n the diffraction order. For the 002-plane being the lattice plane with the highest reflected intensity, the lattice spacing is known to be $d = 3.354 \text{ \AA}$. K_α fluorescence of iodine is emitted at an energy of $E = 28.6 \text{ keV}$. Therefore the Bragg angle calculates³⁴ to approximately 3.7° . Following a certain convolution procedure³⁵ an upper limit for the energy resolution (FWHM) can be determined by the following equation:

$$E/\Delta E = \tan(\theta)/\Delta\theta. \quad (2)$$

Here ΔE is the energy resolution and $\Delta\theta$ is a quantity called intrinsic width of Bragg reflection, or Darwin width³⁶, with a reported value of 26 arcs for the HOPG 002-plane³⁷. Hence, for the first reflection order of the HOPG crystal ΔE calculates to about 3.2 keV.

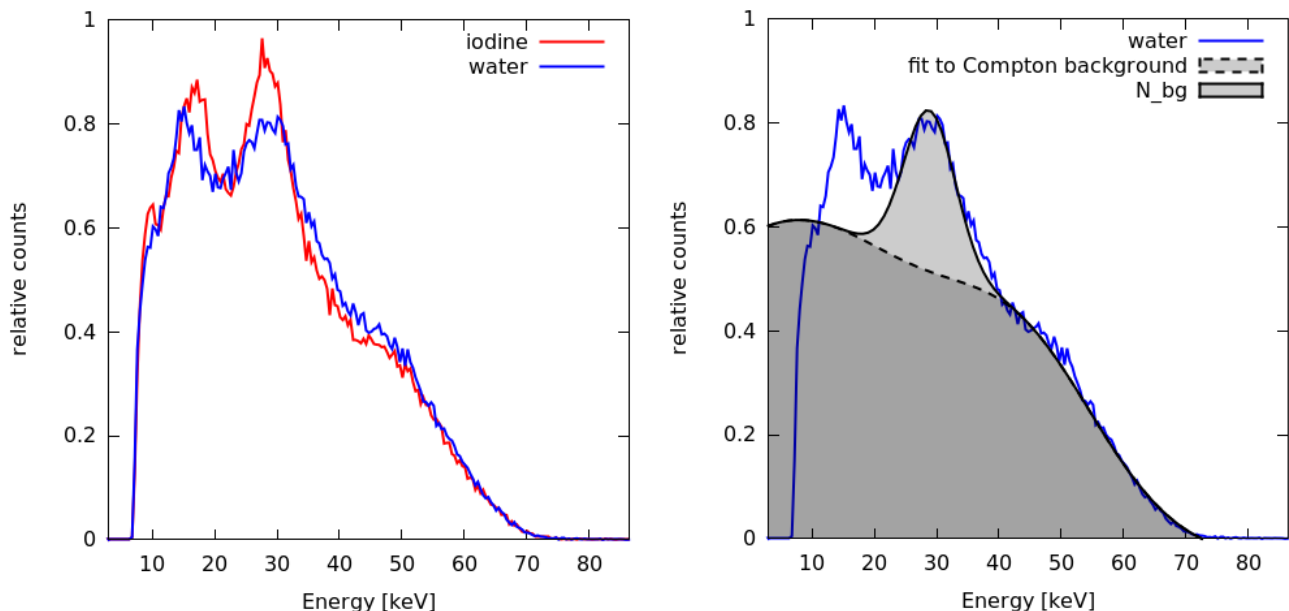


Figure 2: Left: Fluorescence measurements with a phantom containing simple water, also show an increased amount of photons with energies around that of the iodine K_α fluorescence; Right: Approximation to the Compton background with a combination of quadratic functions. All spectra are normalized to the total number of counts.

2.2 XFCT imaging setup

The proposed imaging setup was built on a 50×50 cm Aluminum plate (figure 1) and the isocenter was positioned at a distance of 52 cm from the x-ray tube (Yxlon GmbH, Hamburg, Germany). For XRF detection a NaI scintillation detector (Ortec Inc., Oak Ridge, TN, USA) with a sensitive area of nearly 20 cm^2 and an energy resolution of roughly 7 keV in the energy range of the iodine fluorescence was placed at a 21.5 cm distance from the center, such that the spacing between crystal fan geometry and the envisaged position of the phantom was about 11.5 cm. The energy spectrum was recorded in 1024 energy bins with a bin width of approximately 500 eV. Count rate limitations of 2×10^5 cps, as stated by Ortec, were not exceeded. A head piece made of lead with an opening window of $2 \times 3 \text{ cm}^2$ was attached to the detector's sensitive area, serving as mount and spacer for the analyzer crystal leaves. Thus, the space between the blades was kept constant at 3 mm, while their opposite end directing towards the isocenter converged, leaving a spacing of 0.3 mm. Every blade consists of two parts with dimensions $50 \times 20 \times 3 \text{ mm}^3$ each. The collimating part is made of Al, while the energy selecting part consists of 2 mm thick HOPG material on top of 1 mm Al. This absorber layer underneath the HOPG is important in order to confine the amount of transmitted Compton scattered photons. Both components encompass an angle of 176.3° , providing optimal conditions for the reflection of iodine K_α fluorescence photons.

We used two different kinds of phantoms: In order to test the feasibility of this imaging method, we implemented small test tubes with 20 mm and 5 mm of length and diameter, respectively, and filled them with iodine concentrations of 0.12 % and 0.5 %. As a slightly more complex phantom we used a cylinder composed of PMMA (polymethyl methacrylate) with a length of 60 mm and a diameter of 30 mm. Its interior left space for the above mentioned small test tubes that we filled with iodine solutions with concentrations of 0.9 %, 1.9 %, 3.8 %, and 7.5 %. For tomographic imaging, we placed the phantoms on a manual rotation/translation stage. The x-ray tube with a tungsten anode and an inherent filtration of 4 mm of beryllium was additionally filtered by 0.1 mm Aluminum and operated at a peak kilovoltage of 90 kVp and a tube current of 12.0 mA for each experiment. Thus, the iodine sample was exposed to an estimated³⁸ x-ray dose rate of some mGy/s.

2.3 XFCT data acquisition and reconstruction

For XFCT imaging the filtered polychromatic x-ray beam was collimated to a pencil beam using a hole collimator with a diameter of 1 mm. A system of laser pointers indicating the center of the x-ray tube was used to determine the exact centric position of the phantom within the imaging setup. Afterwards the phantom was translated in x-direction by +15 mm to the starting position for XFCT data acquisition. In steps of 1 mm the phantom was successively translated on the x-axis up to its final position at -15 mm, resulting in 31 translations. For each position a XRF spectrum was recorded for a time of 60 seconds and under equal tube settings, adding up to a scan time of 31 minutes. In order to obtain a complete sinogram the phantom needs to be rotated and the same procedure with 31 translations needs to be repeated for each angular position. Since our phantom was rotationally symmetric and placed centric to the 31 translation steps, we recorded a data set of translations for only one angular position and duplicated the values assuming rotation steps of 5° , resulting in 36×31 data points. The images were reconstructed with the well-known Filtered-Back-Projection (FBP) algorithm for parallel beam projections³⁹ with a resolution of 216×216 and a pixel size of 0.14 mm.

In spite of shielding the imaging system with lead plates of 1 cm thickness, we detected low background counts due to the leakage x-rays from the x-ray source. Therefore we recorded a “zero”-spectrum without phantom and subtracted it from every XRF spectrum of the XFCT experiments.

Following this procedure we investigated two different detector positions. At first, the detector was placed in a 90° angle (fig. 1, l.h.s.) to the primary beam, which is the traditional position for measuring x-ray fluorescence. For the second setup, we placed the detector in the backscatter region, in fact in an angle of 70° to the x-ray source. This has been proven to be advantageous²² since, due to the anisotropic energy distribution of Compton scatter, this region offers a decreased probability of the obfuscation of fluorescence photons.

Each recorded XRF spectrum contains peaks corresponding to the iodine K_α fluorescence, additional reflections of the fan, and background scatter. In order to extract the net XRF counts N_{xrf} from the total amount of photons N_{tot} it is necessary to identify the fraction of background photons N_{bg} and subtract them from the recorded spectra:

$$N_{\text{xrf}} = N_{\text{tot}} - N_{\text{bg}}. \quad (3)$$

This procedure, however, is very complex considering that the energy-selective properties of the crystal fan construction improves the SNR in a preferred region around 28.6 keV, meaning that not only XRF photons are reflected onto the detector's sensitive area, but all photons within this energy range, including those of Compton scattering. As a consequence, spectra acquired from measurements with phantoms containing simple water, also show an increased amount of photons with energies around that of iodine K_{α} fluorescence (cp. figure 2). Therefore the amount of Compton photons N_{bg} cannot be estimated with a simple fit function to the background. In order to resolve this difficulty, we acquired one spectrum using a centric positioned phantom filled with water and estimated the ratio between the area underneath the peak around 28.6 keV and the Compton background (peak-to-background ratio, PBR). The Compton background was approximated with a quadratic fit to the spectrum leaving out the energy parts between 10 and 40 keV, while the fan induced peak was estimated by a Gauss function. For each of the 31 phantom positions, i.e. every spectrum of the acquired XRCT data set, we created a fit function to the background scatter following the same procedure as for the water phantom and added a Gauss function around the fan induced peak according to the estimated PBR. Thus we approximated the portion of Compton scattered photons N_{bg} of every individual XFCT spectrum and extracted the net signal of iodine K_{α} fluorescence (Eq. 3).

3 RESULTS

3.1 Emission spectra

Figure 3 shows the spectra of different iodine concentrations for the 90° scans of the centric position of the smaller simple (l.h.s.) and the more complex PMMA (r.h.s.) phantom together with a fit to the scatter background. All spectra are normalized to the total number of counts. The vast majority of counts arise from multiple scattered Compton photons. It is evident that with increasing tracer concentration not only the fluorescence peaks around 28.6 keV increase, but also up to two peaks in lower energy regions. These peaks do not arise from further iodine fluorescence lines since photons originating from higher order atom shells are situated at energies below 4 keV. The same holds for emission lines of the fan material (Al and Pb), which lay outside the energy region of interest. Also reflections on crystal planes other than the 002-plane can be excluded, since their reflection intensities are too low in order to show a visible effect in the spectrum.

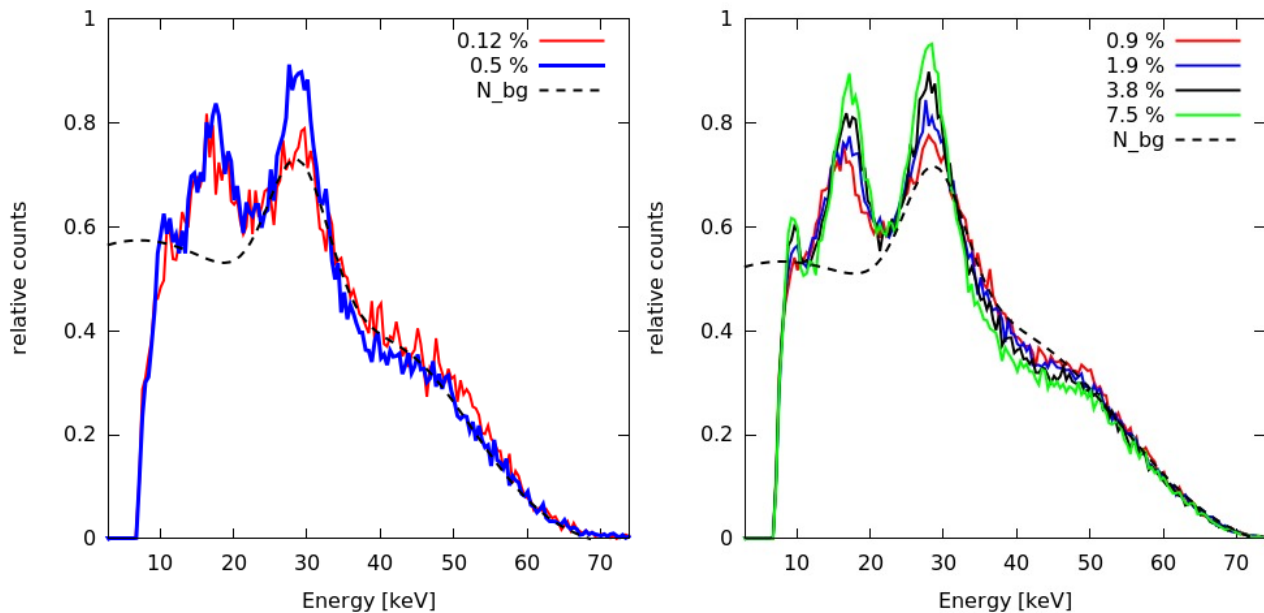


Figure 3: Recorded spectra of different iodine concentrations for the 90° detector configuration of the centric positioned simple phantom (l.h.s.) and the more complex phantom (r.h.s.), including a fit to the background. All spectra are normalized to the total number of counts.

Another explanation is that multiple scattered Compton photons with energies in the range of the undefined peaks are reflected on the 002-plane of the crystal. This idea can however be discarded for two reasons: A photon carrying an energy of about 18 keV needs to hit the HOPG surface with an angle of incidence of roughly 6°, which is improbable since the radially aligned fan leafs allow for a maximum deviation of ± 0.4° to the envisaged incidence angle of 3.7°. The other reason is that even if Compton photons of lower energies with respective incident angles for optimal reflectivity would reach the crystal surface, the recorded spectrum should display a continuous distribution instead of discrete peaks at selected energies. It is however certain that these undefined spurious peaks root in the fan structure. Given the fact that their height varies with the iodine concentration, it is most likely that Compton photons – an increased density of the tracer solution leads to increased Compton scattering – are impaired by further scattering within the fan construction before they are directed onto the detector’s sensitive area. However, as these additional peaks are sufficiently separated from the main fluorescence peak in the energy spectrum, the XRF signal is not affected by obfuscation.

A comparison between the two different detector-fan configurations examined in this work is shown in figure 4 for the PMMA phantom including an iodine concentration of 7.5 %. Other than expected from the findings of previous studies^{22,24,25} the XRF spectra acquired from different detector positions show no significant difference concerning the distribution of the Compton photons. This may be a consequence of the fan structure, which is optimized to suppress the background noise in two ways, namely by angular filtering of non-radially directed Compton scatter and by absorbing photons with an energy other than that of about 28.6 keV. Although our results do not confirm the expectations, it can be concluded that the SNR remains independent of the angular detector-fan position. Therefore a simultaneous data acquisition with both configurations is practicable in order to improve the image quality. This is a consequence of the inverse proportionality between the solid angle and the radiation dose:

$$\text{Solid angle} \sim 1/\text{Dose}. \tag{4}$$

Hence, extending the sensitive detector area allows for a significant reduction of radiation dose.

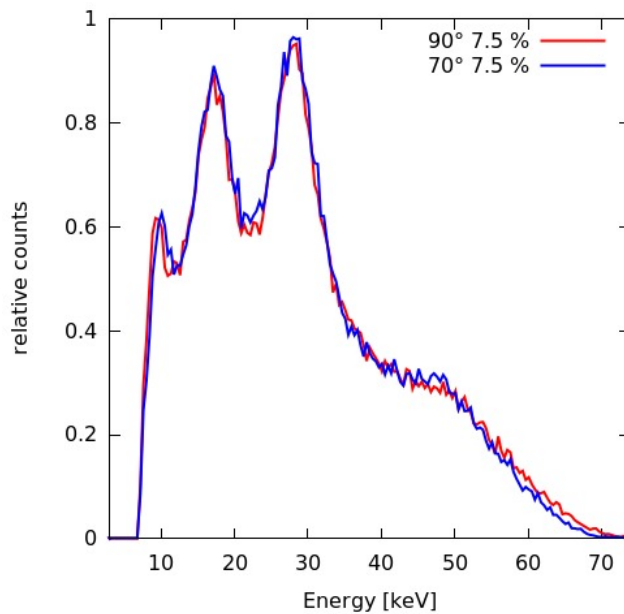


Figure 4: Comparison of the XRF spectra of the centric positioned large phantom containing an iodine concentration of 7.5 %, recorded in the conventional 90° detector-fan position and the 70° configuration. The spectra show no significant difference with regard to the distribution of the Compton photons.

3.2 XFCT images

Figure 5 displays a sinogram of a data set recorded in the 90° angular detection configuration for the large PMMA phantom with an iodine concentration of 7.5 %. Its simplified shape of a vertical bar derives from the rotational symmetry of the phantom and the scanning geometry. An important aspect is that a higher amount of signal was recorded when the phantom was translated in the positive section of the x-axis, in comparison to a decreased signal yield when the phantom was placed at negative x-values. This discrepancy can be explained by the circumstance that in the former case the photons have to pass through the phantom where they are subject to absorption and scattering before they reach the crystal fan and sensitive detector area. The consequences of the asymmetric signal distribution are clearly visible in the reconstruction images in figure 6 for the small phantom and figure 7 for the PMMA phantom. Independent of phantom type and tracer concentration a large amount of artefacts appears in all reconstructed slices. In order to correct for this side effect it would be necessary to acquire complementary XFCT data sets in opposite angular detector position, i.e. in -70° and -90°. Further contributions to the correction of artefacts can be accomplished with data of an absorption image. Nevertheless, the reconstructed slices in this work clearly display the position of the iodine solution within the phantom, albeit in varying degrees of contrast. The images of both phantoms show that with decreasing tracer concentration the boundaries of the tube containing the iodine solution become increasingly undefined, which however could be corrected by increasing the scanning resolution. As already derived from the emission spectra comparing the angular detector-fan position (figure 4), the reconstructed images show no preference in angular detection configuration with respect to the XRF yield. The combination of both data sets nonetheless leads to an increase in contrast which again confirms the correlation between the size of the detector area and XRF signal yield.

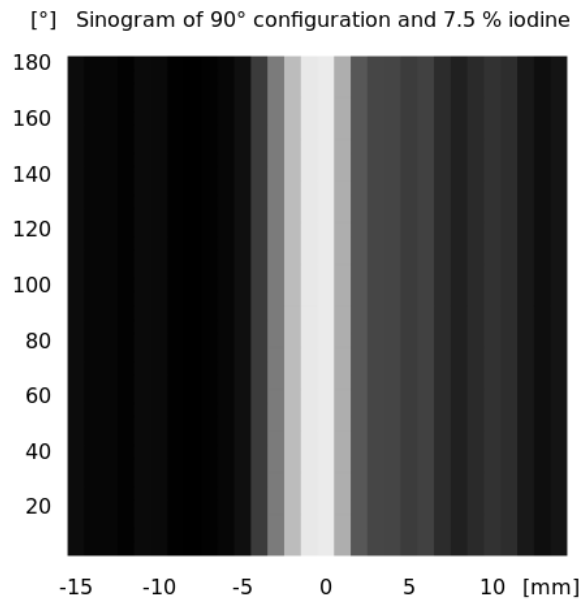


Figure 5: Sinogram of a data set recorded in the 90° angular configuration for the large PMMA phantom with an iodine concentration of 7.5 %. The vertical bar derives from the rotational symmetry of the phantom and the detection geometry. An increased amount of signal is measured for a phantom position at positive values on the x-axis, whereas the signal is decreased when the phantom is placed at negative x-values.

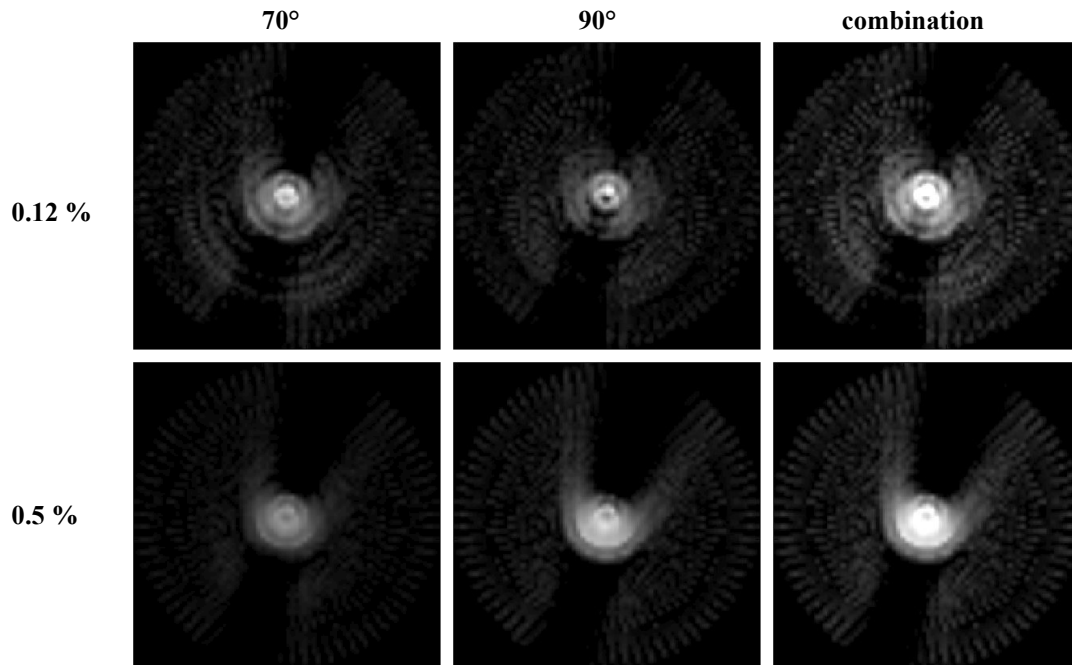


Figure 6: XFCT reconstruction images of the small phantom for the detector configurations 70°, 90°, and their combination, with iodine concentrations of 0.12 % and 0.5 %.

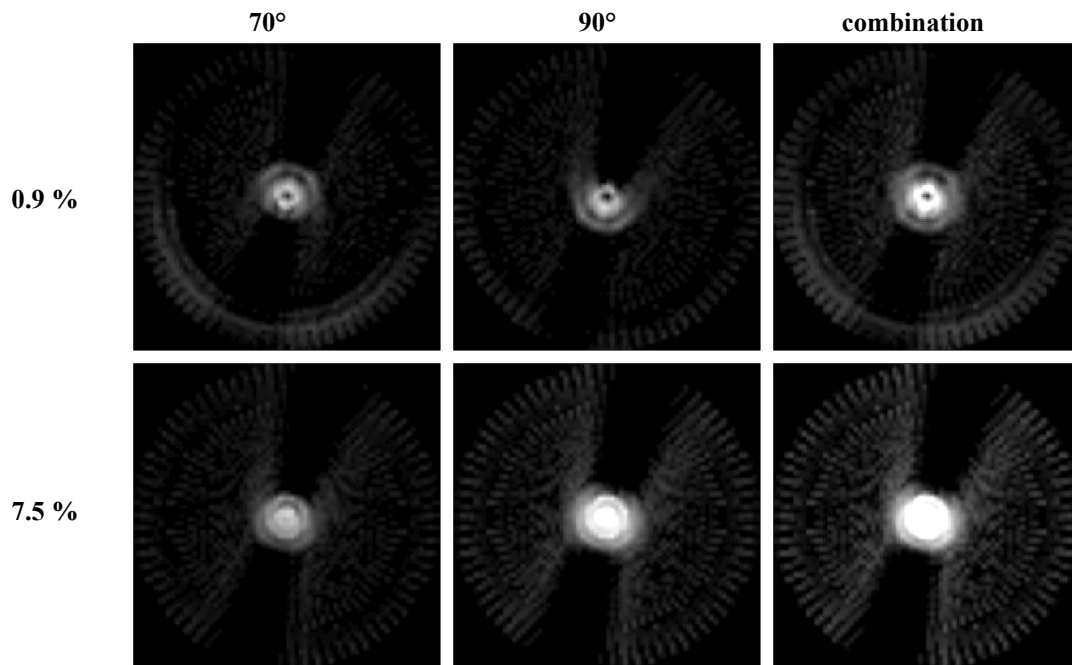


Figure 7: XFCT reconstruction images of the PMMA phantom for the detector configurations 70°, 90°, and their combination, with iodine concentrations of 0.9 % and 7.5 %.

4 DISCUSSION AND OUTLOOK

In this work we investigated the feasibility of an imaging setup for x-ray fluorescence computed tomography (XFCT) with an energy-selective analyzer crystal fan together with polychromatic x-ray sources and large area detectors with a moderate energy resolution. This fan construction consists of an array of five radially aligned blades composed of Al and HOPG crystal material. The Al section works as collimator filtering out non-radially directed multiple-scattered Compton photons, whereas the HOPG acts as supplementary energy filter that preferably reflects photons within the energy range of the iodine K_{α} fluorescence and tends to suppress those of different energies. This energy-selecting property enables the implementation of detectors with large sensitive areas that generally show a deficiency in energy resolution, but record a significantly increased amount of the isotropically emitted XRF signal. As opposed to other approaches^{e.g. 8,9,11} where in favor of an adequate energy resolution and a decreased detection of background noise a small area detector was used, the fan device suppresses spurious Compton photons and hence prevents count rate problems.

With a polychromatic filtered x-ray source set to 90 kV and 12 mA resulting in an estimated dose rate of a few mGy/s, we have shown that within a scan time of 60 seconds an iodine concentration of 0.12 % can be detected in a simple phantom. Implementing a more complex phantom, consisting of a PMMA cylinder filled with iodine solutions of various concentrations, the lowest discriminable concentration was 0.9 %. XFCT reconstruction images of both phantoms showed that with decreasing tracer concentration and hence decreasing image contrast the boundaries of the iodine containing tube become increasingly undefined. This is an effect of the scanning resolution, which will be raised in future investigations. Moreover, additional XFCT data of complementary detector configurations as well as an absorption image would provide corrections to the reconstruction process and thus resolve the uncertainties of spatial discrimination.

We also compared two particular detector configurations where the detector-fan construction was placed in a 90° angle to the x-ray source and in the backscatter region at 70°. Other than indicated in various studies^{22,24,25}, we were not able to confirm the differences between orthogonal and backscatter angular detection position, where due to the anisotropic behavior of Compton scattering the latter configuration should show a shift of the Compton peak to lower energies in the XRF spectra. This discrepancy to other studies may be an effect of the fan which is mainly responsible for the suppression of the Compton signal. A combination of both setups, however noticeably improved the image contrast, which due to the inverse proportionality between solid angle and radiation dose permits for a dose reduction while maintaining the same sensitivity. Nevertheless it is worthwhile to scrutinize various detector-fan configurations in future experiments, since adjustments to the fan considering the individual demands of each angular position could optimize the XRF signal yield.

A major drawback of this imaging setup is the large scan time needed for XFCT reconstruction images because of the utilization of a pencil beam, which however is crucial to the detection resolution. In this work the chosen spatial resolution of 1 mm together with 31 translation steps resulted in a total scanning time of 31 minutes for one slice of a mouse-sized object, which impedes the practical application to *in vivo* imaging. An increase of the x-ray flux together with a higher contrast agent concentration decreases the scanning time, but requires larger detector areas in order to maintain an acceptable radiation dose.

Another disadvantage of this imaging setup is that it cannot readily be utilized in combination with contrast agents based on high-Z elements larger than iodine. This is due to the HOPG structure which shows a decrease in integral reflectivity and energy resolution with increasing photon energies. Gold, for example, requires a Bragg angle of 1.54° for an optimal reflection of K_{α} fluorescence, which calculates to a width of the reflection of 18.5 keV (FWHM) and an integral reflectivity of 20 %. For tracers containing AuNPs, which are of particular interest in recent research in connection with XFCT, using the HOPG crystal for energy selection is therefore impractical. A fan construction using a different crystal structure with a smaller mosaic spread or a bent monocrystal would be more practical for gold.

If the mentioned obstacles can be overcome, this imaging setup provides an approach towards XFCT imaging in a large solid angle with high detection sensitivities and low radiation doses. Especially the extension of our imaging setup to the detection of AuNPs appears to be pivotal with regard to molecular imaging in humans.

ACKNOWLEDGEMENTS

The authors would like to thank Matthias Greiter for fruitful discussions and technical help with the x-ray tube and Oleg Tischenko for help with the FBP algorithm.

REFERENCES

- [1] Schlomka, J. P., Roessler, E., Dorscheid, R., Dill, S., Martens, G., Istel, T., Bäumer, C., Herrmann, C., Steadman, R., Zeitler, G., Livne, A., and Proska, R., "Experimental feasibility of multi-energy photon-counting K-edge imaging in preclinical computed tomography," *Phys. Med. Biol.*, 53(15), 4031-4031 (2008).
- [2] Daniel, M.-C., Astruc, D., "Gold nanoparticles: Assembly, supramolecular chemistry, quantum-size-related properties, and applications toward biology, catalysis, and nanotechnology," *Chem. Rev.* 104(1), 293-346 (2004).
- [3] Connor, E. E., Mwamuka, J., Gole, A., Murphy, C. J., and Wyatt, M. D., "Gold nanoparticles are taken up by human cells but do not cause acute cytotoxicity," *Small*, 1(3), 325-327 (2005).
- [4] Hainfeld, J. F., Slatkin, D. N., Focella, T. M., and Smilowitz, H. M., "Gold nanoparticles: A new x-ray contrast agent," *Br. J. Radiol.*, 79(939), 248-253 (2006).
- [5] Kim, D., Park, S., Lee, J. H., Jeong, Y. Y., and Jon, S., "Antibiofouling polymer-coated gold nanoparticles as a contrast agent for in vivo x-ray computed tomography imaging," *J. Am. Chem. Soc.*, 129(24), 7661-7665 (2007).
- [6] Popovtzer, R., Agrawal, A., Kotov, N. A., Popovtzer, A., Balter, J., Carey, T. E., and Kopelman, R., "Targeted gold nanoparticles enable molecular CT imaging of cancer," *Nano Letters*, 8(12), 4593-4596 (2008).
- [7] Hainfeld, J. F., O'connor, M. J., Dilmanian, F. A., Slatkin, D. N., Adams, D. J., and Smilowitz, H. M., "Micro-CT enables microlocalisation and quantification of Her2-targeted gold nanoparticles within tumour regions," *Br. J. Radiol.*, 84(1002), 526-533 (2010).
- [8] Cesareo, R., and Mascarenhas, S., "A new tomographic device based on the detection of fluorescent x-rays," *Nucl. Instrum. Methods Phys. Res.*, 277(2), 669-672 (1989).
- [9] Takeda, T., Wu, J., Lwin, T.-T., Huo, Q., Yuasa, T., Hyodo, K., Dilmanian, F. A., and Akatsuka, T., "X-ray fluorescent CT imaging of cerebral uptake of stable-iodine perfusion agent iodoamphetamine analog IMP in mice," *J. Synchrotron Radiat.*, 16(1), 57-62 (2009).
- [10] Müller, B. H., Hoeschen, C., Grüner, F., Arkadiev, V. A., and Johnson, T. R. C., "Molecular imaging based on x-ray fluorescent high Z-tracers," *Phys. Med. Biol.*, 58(22), 8063-8076 (2013).
- [11] Bazalova, M., Kuang, Y., Pratz, G., and Xing, L., "Investigation of x-ray fluorescence computed tomography (XFCT) and K-edge imaging," *IEEE Trans. Med. Imag.*, 31(8), 1620-1627 (2012).
- [12] Cheong, S.-K., Jones, B. L., Siddiqi, A. K., Liu, F., Manohar, N., and Cho, S. H., "X-ray fluorescence computed tomography (XFCT) imaging of gold nanoparticle-loaded objects using 110 kVp X-rays," *Phys. Med. Biol.*, 55(3), 647-662 (2010).
- [13] Cong, W., Shen, H., Cao, G., Liu, H., and Wang, G., "X-ray fluorescence tomographic system design and image reconstruction," *J. X-ray Sci. Technol.*, 21(1), 1-8 (2013).
- [14] Jones, B. L., Manohar, N., Reynoso, F., Karellas, A., and Cho, S. H., "Experimental demonstration of benchtop x-ray fluorescence computed tomography (XFCT) of gold nanoparticle-loaded objects using lead-and tin-filtered polychromatic cone-beams," *Phys. Med. Biol.*, 57(23), 457-467 (2012).

- [15] Hertz, H. M., Larsson, J. C., Lundstrom, U., Larsson, D. H., and Vogt, C., "Laboratory x-ray fluorescence tomography for high-resolution nanoparticle bio-imaging," *Opt. Lett.*, 39(9), 2790-2793 (2014).
- [16] Feng, P., Cong, W., Wei, B., and Wang, G., "Analytic comparison between x-ray fluorescence CT and K-edge CT," *IEEE Trans. Biomed. Eng.*, 61(3), 975-985 (2014).
- [17] Geraki, K., Farquharson, M. J., and Bradley, D. A., "Concentrations of Fe, Cu and Zn in breast tissue: A synchrotron XRF study," *Phys. Med. Biol.*, 47(13), 2327-2339 (2002).
- [18] Rizk, S. L. and Skyepeck, H. H., "Comparison between concentrations of trace-elements in normal and neoplastic human-breast tissue," *Cancer Res.*, 44(11), 5390-5394 (1984).
- [19] Geraki, K., Farquharson, M. J., and Bradley, D. A., "X-ray fluorescence and energy dispersive x-ray diffraction for the quantification of elemental concentrations in breast tissue," *Phys. Med. Biol.*, 49(1), 99-110 (2004).
- [20] Di, W., Yuhua, L., Wong, M. D., and Hong, L., "A method of measuring gold nanoparticle concentrations by x-ray fluorescence for biomedical applications," *Med. Phys.*, 40(5), 051901 (2013).
- [21] Boisseau, P. and Grodzins, L., "Fluorescence tomography using synchrotron radiation at the NSLS," *Hyperfine Interactions*, 33(1), 283-292 (1987).
- [22] Ahmad, M., Bazalova-Carter, M., Fahrig, R., and Xing, L., "Optimized detector angular configuration increases the sensitivity of x-ray fluorescence computed tomography (XFCT)," *IEEE Trans. Med. Imag.*, 34(5), 1140-1147 (2015).
- [23] Manohar, N. et al., "Quantitative imaging of gold nanoparticle distribution in a tumor-bearing mouse using benchtop x-ray fluorescence computed tomography," *Sci. Rep.* 6, 22079 (2016).
- [24] Ahmad, M., Bazalova, M., Xiang, L., and Xing, L., "Order of magnitude sensitivity increase in x-ray fluorescence computer tomography (XFCT) imaging with an optimized spectro-spatial detector configuration: Theory and simulation," *IEEE Trans. Med. Imag.*, 33(5), 1119-1128 (2014).
- [25] von Busch, H., Harding, G., Martens, G., Schlomka, J.-P., and Schweizer, B., "Investigation of externally activated x-ray fluorescence tomography for use in medical diagnostics," *Proc. SPIE* 5745, 90-101 (2005).
- [26] Beckhoff, B., Kanngießer, B., Langhoff, N., Wedell, R., and Wolff, H. H., [Handbook of Practical X-Ray Fluorescence Analysis], Springer, Berlin, 199-302 (2006).
- [27] Bazalova, M., Ahmad, M., Pratz, G., and Xing, L., "L-shell x-ray fluorescence computed tomography (XFCT) imaging of cisplatin," *Phys. Med. Biol.*, 59(1), 219-232 (2014).
- [28] Karanfil, C., Zhong, Z., Chapman, L. D., Fischetti, R., Bunke, G. B., Segre, C. U., and Bunker, B. A., "A bent Laue analyzer detection system for dilute fluorescence XAFS," *AIP Proc.* 521(1), 178-182 (2000).
- [29] Moore, A. W., [Chemistry and Physics of Carbon Vol. 11], Marcel Dekker, New York, 69-187 (1973).
- [30] Agostinelli, S., et al, "Geant4: a simulation toolkit," *Nucl. Instrum. Methods Phys. Res.* 506(3), 250-303 (2003).
- [31] Müller, B. H., Hoeschen, C., Grüner, F., and Johnson, T. R. C., "X-ray fluorescence molecular imaging of high-Z tracers: investigation of a novel analyzer based setup," *Proc. SPIE*, 90331J (2014).
- [32] Green, F. H., Veale, M. C., Wilson, M. D., Seller, P., Scuffham, J., and Pani, S., "Scatter free imaging for the improvement of breast cancer detection in mammography," *Phys. Med. Biol.* 61(20), 7246-7262 (2016).

- [33] Sanchez del Rio, M., Gambaccini, M., Pareschi, G., Taibi, A., Tuffanelli, A., and Freund, A., "Focusing properties of mosaic crystals," Proc. SPIE 3448, 246-255 (1998).
- [34] Sanchez del Rio, M. and Dejus, R. J., "Status of XOP: an x-ray optics software toolkit," Proc. SPIE 5536, 171-174 (2004).
- [35] Legall, H., Stiel, H., Arkadiev, V., and Bjeoumikhov, A. A., "High spectral resolution x-ray optics with highly oriented pyrolytic graphite," Opt. Expr. 14(10), 4570-4576 (2006).
- [36] Zachariasen, W. H., [Theory of X-Ray Diffraction in Crystals], Dover, Meneola N.Y., 159-175 (1945).
- [37] Ice, G. E. and Sparks C. J., "Mosaic crystal x-ray spectrometer to resolve inelastic background from anomalous scattering experiments," Nucl. Instrum. Methods Phys. Res. 291(1), 110-116 (1990).
- [38] Poludniowski, G., Landry, G., DeBlois, F., Evans, P.M., Verhaegen, F., "SpekCalc: a program to calculate photon spectra from tungsten anode x-ray tubes," Phys. Med. Biol. 54(19), 433-438 (2009).
- [39] Kak, A.C. and Slanley, M., [Principles of computerized tomographic imaging], Society of Industrial and Applied Mathematics, 49-75 (2001).